Hydration mechanisms of tungsten trioxide revealed by water adsorption isotherms and first-principles molecular dynamics simulations

Y. Foucaud, Azza Ben Jannet, Stefano Caramori, Rafael Canevesi, Moncef Said, Alain Celzard, Vanessa Fierro, Michael Badawi, Mariachiara Pastore

Hydration mechanisms of tungsten trioxide revealed by water adsorption isotherms and first-principles molecular dynamics simulations

Yann Foucaud,[1,*] Azza Ben Jannet,[1,2] Stefano Caramori,[3] Rafael Canevesi,[4] Moncef Said,[2] Alain Celzard,[4,5] Vanessa Fierro,[4] Michael Badawi,[1,*], Mariachiara Pastore[1,*]

[1] Université de Lorraine, CNRS, Laboratoire de Physique et Chimie Théoriques (LPCT), F-54000, Nancy, France

[2] Université de Monastir, Faculté des Sciences de Monastir, Laboratoire de la Matière Condensée et des Nanosciences (LMCN), LR11ES40, Avenue de l'Environnement, 5000, Monastir, Tunisie

[3] Dipartimento di Scienze Chimiche, Farmaceutiche ed Agrarie, 44121 Ferrara, Italy

[4] Université de Lorraine, CNRS, Institut Jean Lamour (IJL), F-88000 Épinal, France

[5] Institut Universitaire de France (IUF)

Corresponding authors: yann.foucaud@univ-lorraine.fr; michael.badawi@univ-lorraine.fr ; mariachiara.pastore@univ-lorraine.fr

Keywords: γ-Monoclinic WO_3, surface defects, water adsorption, photocatalysis, DFT

Abstract

WO_3 is one of the most interesting materials for photocatalysis due to its optical absorption in the UV-Vis, good charge carriers transport and stability against photocorrosion. A detailed knowledge of the hydration state of WO_3 is indispensable to gain more precise mechanistic insights into its photocatalytic activity. To the best of our knowledge, the hydration process of WO_3 has been scarcely studied so far and only from a theoretical point of view, mostly by means

of static density functional theory (DFT) calculations. Here, we use manometric gas sorption experiments combined with extensive *ab initio* molecular dynamics simulations to investigate the hydration mechanisms of WO_3 at room temperature. We demonstrate that water adsorbs molecularly in a two-step mechanism: the first water sub-layer interacts with the under-coordinated surface tungsten atoms through electrostatic interactions, and, in a second step, a full layer is formed through hydrogen bonds established with the pre-adsorbed water molecules and with the under-coordinated surface oxygen atoms. The computed value of -90 $kJ \cdot mol^{-1}$ for the isosteric enthalpy of adsorption of the first water molecules is in excellent agreement with the experimental value estimated using the Clausius-Clapeyron approach from the experimental adsorption isotherms. The isosteric enthalpy of adsorption steadily decreases in absolute value when the surface coverage is increased to tend towards the enthalpy of condensation of water after three adsorption layers.

1. Introduction

To meet the world's growing demand for energy, the adoption of hydrogen-based technologies would provide large amounts of energy from clean and inexhaustible resources, such as sunlight and water. Since the first example of light-driven water splitting reported in 1972 by Fujishima and Honda using a titanium dioxide (TiO_2) photoanode irradiated with UV light,[1] heterogeneous photoelectrochemical (PEC) water splitting has attracted increasing scientific and technological interest.[2–4] TiO_2 nanoparticles (NPs) remain the most efficient photocatalytic materials,[5] although the need for UV light hinders their use in large-scale, solar-driven water splitting, as only a small fraction of the sun's UV radiation reaches the Earth's surface. Various oxide nanomaterials, such as SnO_2, ZnO, and WO_3 have been also used, although their systematic use and detailed characterization are still lacking in the literature.[6]

In this context, tungsten trioxide (WO_3)-based nanomaterials offer remarkable characteristics: they are earth-abundant, non-toxic, and highly resistant to photo-corrosion under acidic conditions.[7,8] All these properties make WO_3 relevant for many technological applications, such as photocatalysis,[9–15] electrochromic devices,[16,17] and gas sensors.[18–20] Moreover, the experimental band gap of WO_3 is in the range of 2.5-3.0 eV,[21] significantly smaller than the corresponding value of TiO_2, which is in the 3.0-3.2 eV range.[22] Consequently, WO_3 can, in

principle, be efficient in absorbing visible light, thus overcoming the main limitation of TiO_2.[23–25]

Given these appealing advantages as a standalone or combined photocatalyst in various heterojunctions, WO_3 has been the subject of many experimental[26–29] and theoretical studies[30–40] in recent years. In particular, the solid/liquid interfacial properties, crucial for the efficiency of photocatalytic processes,[41–54] have been theoretically investigated in the case of the WO_3/water interface.[41,55,56] Previous computational studies have indeed addressed the fundamental understanding of the adsorption of water molecules on the γ-(001) surface [hereafter indicated as (001)].[41,46,55,56] Most of the reported works have shown that water adsorbs preferentially in a molecular (undissociated) form, since under-coordinated W atoms at the (001) surface are Lewis acids able to coordinate a water molecule.[46]

Recently, the dissociation of water on the WO_3 surface has been experimentally studied using *operando* diffuse reflectance infrared Fourier transform (DRIFT) spectroscopy and resistance measurements coupled with exhaust measurements.[57] No hydroxyl groups were observed at any temperature on the DRIFT spectra of WO_3,[58,59] unlike most other metal oxides, indicating the absence of dissociative adsorption of water molecules on the WO_3 surface. Moreover, the detected increase in the baseline resistance as a function of humidity demonstrated the direct oxidation of the surface by water without the formation of reaction intermediates (*e.g.*, hydroxyl groups).[58–60] In fact, using *ab initio* atomistic thermodynamic calculations, Hurtado et al.[55] demonstrated that above the temperature of 300 K, all water molecules are expelled from the surface.

In this work, we want to elucidate the hydration mechanism of the most stable surface of WO_3, and at assessing the water adsorption enthalpies as a function of coverage at room temperature. To this end, we have investigated the interaction between the (001) WO_3 surface and water using manometric gas sorption experiments combined with dispersion-corrected density functional theory (DFT) calculations. The experimental results allowed us to extract information on the surface heterogeneity in terms of adsorption sites and surface coverage, as well as to determine the isosteric adsorption enthalpy of water as a function of coverage. Besides, we analyzed the atomistic interfacial properties and their evolution during the hydration of the WO_3 surface, by progressively adsorbing undissociated water molecules in the gas phase, and while describing the

surroundings by a continuum solvent. The dynamic behavior of the water/WO_3 interface was also studied using DFT-based molecular dynamics (DFT-MD) simulations at 300 K, from which theoretical isosteric hydration enthalpies for the gradual hydration of the surface were calculated.

2. Material and methods

2.1. Material and its characterization

Material synthesis

WO_3 powder was prepared by precipitation of $WO_3 \cdot H_2O$, followed by thermal dehydration to form WO_3. First, 20 mL of a 37 wt.% HCl solution were added dropwise under magnetic stirring to a 100 mL solution of Millipore water (> 18 MΩ·cm) containing 2.5 g of Na_2WO_4 dissolved in it. The obtained yellowish gelatinous H_2WO_4 precipitate was washed with Millipore water through three cycles of ultrasonic dispersion followed by centrifugation. The collected solid was dried at 323 K overnight in air before conversion to crystalline WO_3, which was carried out at 823 K for 1 hour in air. Finally, the resulting greenish yellow powder was finely ground mechanically with a ball mill for several minutes.

Particle size distribution

The volume size distribution of WO_3 particles was measured by laser diffraction using a Malvern Mastersizer Hydro 2000MU analyzer. The measurement was repeated 4 times and the determination of the characteristic diameters, d_{90}, d_{50} and d_{10}, was done using the average values of each measurement. In the following, $d_x = y$ µm means that x% of the particles have a diameter smaller than y µm.

Tramission electron microscopy

Transmission electron microscopy (TEM) studies were performed using a JEM – ARM 200F Cold FEG TEM/STEM operating at 200 kV and equipped with a spherical aberration (Cs) probe and image correctors (point resolution of 0.12 nm in TEM mode and 0.078 nm in STEM mode).

Simulated selected area electron diffraction (SAED) patterns were generated from the TEM images using fast Fourier-filtering (FFT).

X-Ray diffraction analyses

XRD measurements were performed using a PanAnalytical X'Pert Pro MRD diffractometer equipped with a high resolution 4-circle goniometer, to accurately orient the samples, and with a Mo anticathode (Mo Kα radiation; λ = 0.70930 Å). Rietveld refinement was attempted using diffraction peaks from the orthorhombic and monoclinic phases of WO_3.

2.2. Adsorption experiments

Specific surface area

Textural characterization of the WO_3 sample was performed by N_2 adsorption-desorption at 77 K using a 3-FLEX automated device after degassing at 623 K for 24 h in a Smart VacPrep device, both supplied by Micromeritics. Additional degassing at the same temperature for 12 h was carried out before analysis. A low-pressure dose of 0.01 $cm^3 \cdot g^{-1}$ STP was set to a relative pressure, p/p_0, of 0.1 to obtain the high-resolution N_2 isotherms. N_2 adsorption-desorption was conducted three times to minimize the experimental error. All data were processed with the MicroActive 5.01 software, also provided by Micromeritics. The BET area was determined in the adequate pressure range, taking into account the Rouquerol criteria.[61]

Water adsorption isotherms

High-resolution water isotherms were acquired using ultrapure water (> 18 MΩ·cm) as the vapor source at four different temperatures (285, 295, 305 and 315 K) and up to saturation pressure (p_0) in an automatic BELSORP-max II-HV apparatus (BEL). Prior to weighing, the WO_3 sample was degassed for water adsorption as was done previously for N_2 adsorption-desorption analysis. Vapor uptakes for p/p_0 ranging from 10^{-4} to 0.95 were recorded, and extremely good experimental reproducibility, with differences less than 1%, was confirmed by repeating the water adsorption at a selected temperature of 295 K.

Calculation of the isosteric enthalpy of adsorption

The isosteric enthalpy of adsorption, ΔH_{ads}, corresponds to the heat involved – most often released – when a molecule adsorbs onto a given surface at a given surface coverage.[62] This quantity is negative when the adsorption is exothermic, as in most cases, and can be determined from several adsorption isotherms acquired at different temperatures within, however, a limited temperature range. Generally speaking, ΔH_{ads} can be derived using the Clausius-Clapeyron equation from pressure (p)-uptake (n) data pairs with the same uptake at each temperature,[63] as follows:

$$\Delta H_{ads}(n) = -R \cdot \ln\left(\frac{p_2}{p_1}\right) \frac{T_1 \cdot T_2}{(T_2 - T_1)} \quad (1)$$

where $\Delta H_{ads}(n)$, T_1, T_2, p_1, p_2, n, and R are the isosteric enthalpy of adsorption ($J \cdot mol^{-1}$) at a given occupancy, the temperatures (K), the equilibrium pressures (bar), the uptake ($mol \cdot kg^{-1}$), and the ideal gas constant ($8.314\ J \cdot mol^{-1} \cdot K^{-1}$), respectively. Following the Clausius-Clapeyron approach, the isosteric enthalpy of adsorption is the slope of the curve of $\ln(p)$ versus $(1/T)$ for a given uptake n and can therefore be determined either from experimental or fitted isotherms.[63]

For the calculation of ΔH_{ads} based on experimental isotherms, the equilibrium pressure at a given uptake was determined by interpolating the isotherms between the experimental points using cubic-spline functions. The range of uptakes was discretized and, for each point, ΔH_{ads} was calculated using the Clausius-Clapeyron equation (Eq. 1). Besides, when adsorption models were used, we systematically applied the dual-site Freundlich-Langmuir (DSFL) equation to fit the experimental models with good accuracy. This model combines the robustness of the Langmuir isotherm[64] with a better description given by the Freundlich isotherm[65] for high equilibrium pressures, and considers the possible existence of multiple adsorption sites.[66] The general equation for the DSFL adsorption model is:

$$n = \frac{a_1 \cdot b_1 \cdot p^{c_1}}{1 + b_1 \cdot p^{c_1}} + \frac{a_2 \cdot b_2 \cdot p^{c_2}}{1 + b_2 \cdot p^{c_2}} \quad (2)$$

where n is the adsorbed amount ($mol \cdot kg^{-1}$), p (bar) is the equilibrium pressure (bar), a ($mol \cdot kg^{-1}$) is the maximum uptake, b (bar^{-c}) is the affinity constant between the adsorbent and the adsorbate, and c (dimensionless) is the heterogeneity exponent. The four considered experimental isotherms were fitted using the Levenberg-Marquardt method[67,68] as implemented in SciPy.[69] After the fitting procedure, the equations were rearranged to express the equilibrium pressure as a function

of the uptake and the model parameters, and ΔH_{ads} was calculated using the Clausius-Clapeyron equation (Eq. 1).

2.3. Atomistic simulations

Computational details

All calculations were performed using the Vienna *ab initio* simulation package (VASP)[70] with the projector augmented wave (PAW) method.[71,72] The semilocal Perdew-Burke-Ernzerhof (PBE) exchange-correlation functional[73] in the generalized gradient approximation was used for the calculations, along with the D3-BJ correction of Grimme and coworkers[74] for the dispersion forces. The following orbitals were treated as having valence electrons: $1s^1$ for hydrogen, $5s^2\ 5p^6\ 6s^2\ 5d^4$ for tungsten, and $2s^2\ 2p^4$ for oxygen. The Kohn-Sham equations[75,76] were solved self-consistently until the energy difference between consecutive cycles became less than 10^{-7} eV, using a Gaussian smearing of 0.05 eV to facilitate convergence of the total energy. The geometry was optimized until all forces were less than 0.02 $eV \cdot Å^{-1}$. All calculations were performed at the Gamma point, considering the large size of the cell, with a plane-wave basis set energy cutoff of 500 eV. DFT-based molecular dynamics (DFT-MD) simulations were carried out in the *NVT* ensemble, using the same computational set up, except for the convergence parameter for the Kohn-Sham equations and the energy cutoff, which were reduced to 10^{-5} eV and 400 eV, respectively. The DFT-MD simulations were conducted at a temperature of 300 K, controlled using a Nosé-Hoover thermostat[77–79] with a timestep of 1 fs, and for a total simulation time of 100 ps. Implicit solvation calculations were performed using the Poisson-Boltzmann model to include the dielectric screening effect of the medium as implemented in the VASPsol code,[80,81] with a relative dielectric constant $\varepsilon = 80$ and a Debye length of 3 Å.[80,81]

Structural Model

A primitive unit cell of the WO_3 monoclinic phase (space group $P2_1/n$) containing 32 atoms was used as a starting point.[82] The unit cell was fully relaxed by DFT calculations including the Grimme's D3-BJ correction[74] to obtain lattice parameters a = 7.44 Å, b = 7.58 Å, c = 7.76 Å, $\alpha = \gamma = 90°$ and $\beta = 90.72°$. These data are in good agreement with the experimental values of a = 7.31 Å, b = 7.54 Å, c = 7.69 Å, $\alpha = \gamma = 90°$ and $\beta = 90.90°$.[83] Following previously published

studies, we selected the (001) WO_3 surface with a ($\sqrt{2} \times \sqrt{2}$)-R45° reconstruction,[84] which is known to be the most stable WO_3 surface.[85,86] This reconstructed surface presents a half monolayer of top oxygen atoms, O_t, missing alternately along the *a* and *b* directions, to avoid the presence of any surface dipole,[84] which leads to the coexistence of six-coordinated W atoms, W_{6c}, and five-coordinated W atoms, W_{5c}, on the surface (Figure 1). A slab of W_xO_{3x} with $x = 64$, which corresponds to four layers of W atoms[47,87,88] and a thickness of about 16 Å, was generated from the fully relaxed primitive unit cell, without freezing any layer in the structure optimizations. A vacuum of 15 Å was systematically added above the surface to avoid spurious interactions between the reciprocal surface and the adsorbents along the *c* direction. For calculations involving an isolated water molecule, a cubic box with a side of 30 Å was used to avoid interactions between the molecule and its reciprocal images. Since DFT-MD is computationally demanding, the WO_3 slab was reduced to three layers to conduct these simulations. The two WO_3 slabs considered had an area of 225 $Å^2$; this value was used to calculate the surface coverage and the adsorption layers.

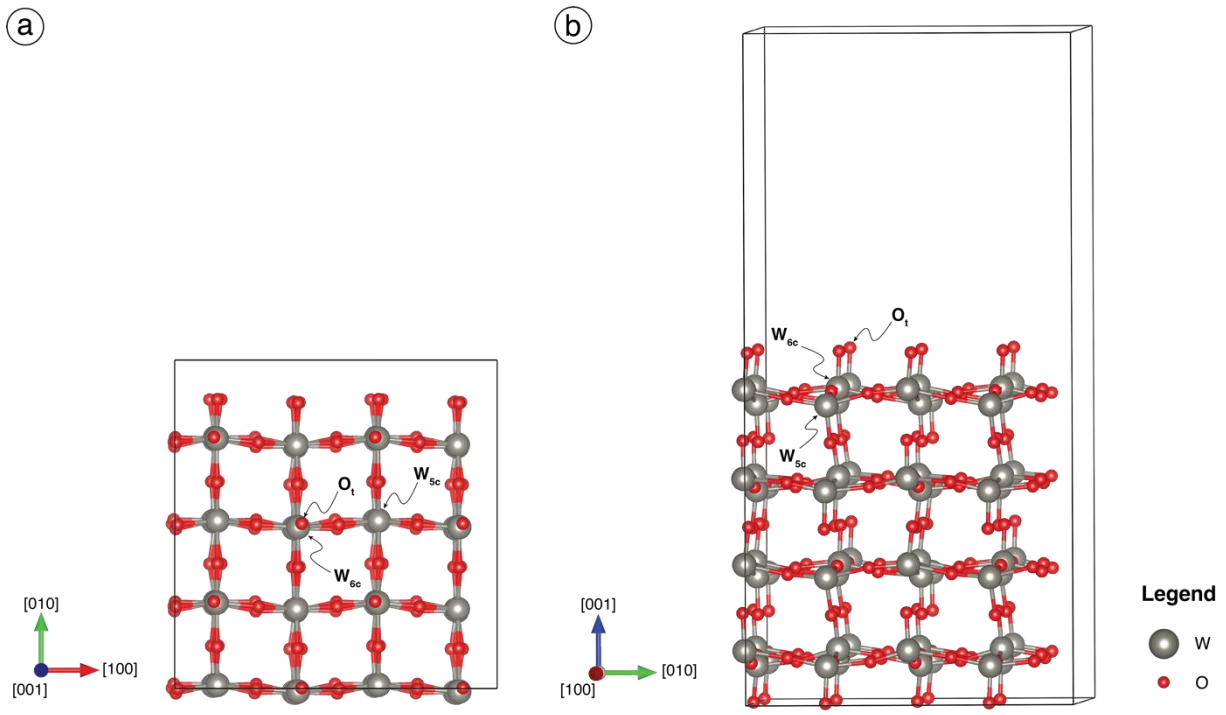

Figure 1. Top view (a) and side view (b) of the cell containing the (001) WO_3 surface, used for the static DFT calculations. For the DFT-MD simulations, the slab was reduced to three layers of tungsten atoms instead of four.

Adsorption energy calculations

When *x* water molecules were adsorbed simultaneously, the total adsorption energy, including the dispersive contribution ($\Delta E_{ads} = \Delta E_{DFT} + \Delta E_{disp}$), was determined as follows:

$$\Delta E_{ads} = E_{x\mathrm{H_2O/WO_3}} - E_{\mathrm{WO_3}} - x \times E_{\mathrm{H_2O}} \quad (3)$$

where $E_{x\mathrm{H_2O/WO_3}}$, $E_{\mathrm{WO_3}}$, and $E_{\mathrm{H_2O}}$ are the total energies of the slab with the *x* adsorbed water molecules, of the bare WO_3 slab, and of the single water molecule in the gas phase, respectively. The adsorption energy per water molecule corresponds to the total adsorption energy, calculated using Eq. 3, divided by the number of adsorbed water molecules, *x*:

$$\Delta E_{ads/molecule} = \frac{\Delta E_{ads}}{x} \quad (4)$$

To acquire a thorough understanding of the hydration mechanisms, progressive hydration was investigated and for this purpose, we calculated the isosteric adsorption energy of *y* molecules for a coverage of *x* water molecules as follows:

$$\Delta E_{ads}^{iso} = \frac{\Delta E_{ads}^{y+x} - \Delta E_{ads}^{x}}{y} \quad (5)$$

where ΔE_{ads}^{x} and ΔE_{ads}^{y+x} are to the total adsorption energies of *x* and *y* + *x* water molecules on the WO_3 surface, respectively. Eq. 5 can also be expressed as a function of the energies of the systems:

$$\Delta E_{ads}^{iso} = \frac{E_{(y+x)\mathrm{H_2O/WO_3}} - E_{x\mathrm{H_2O/WO_3}} - yE_{\mathrm{H_2O}}}{y} \quad (6)$$

where $E_{(y+x)\mathrm{H_2O/WO_3}}$, $E_{x\mathrm{H_2O/WO_3}}$, and $E_{\mathrm{H_2O}}$ represent the total energies of the slab with the *y* + *x* adsorbed water molecules, of the slab with the *x* adsorbed water molecules, and of the single water molecule in the gas phase, respectively. The isosteric enthalpies of adsorption were determined from the DFT-MD simulations, based on Eq. 6, in which each energy term is the total energy of the system averaged over the last 90 ps of the simulation, to exclude a thermalization period of 10 ps.

3. Results and discussion

3.1. Characterization of the WO_3 samples

The particle size distribution of the WO_3 powder synthesized and used in this study was measured (Figure 2). The values of 7.08 ± 1.15, 1.02 ± 0.01, and 0.5 ± 0.01 μm were determined for 90 (d_{90}), 50 (d_{50}), and 10 (d_{10}) % of the particles, respectively. As can be seen in Figure 2, the particle size distribution of the WO_3 powder is bimodal, with a large peak centered at 0.7 μm and a smaller one at 10 μm.

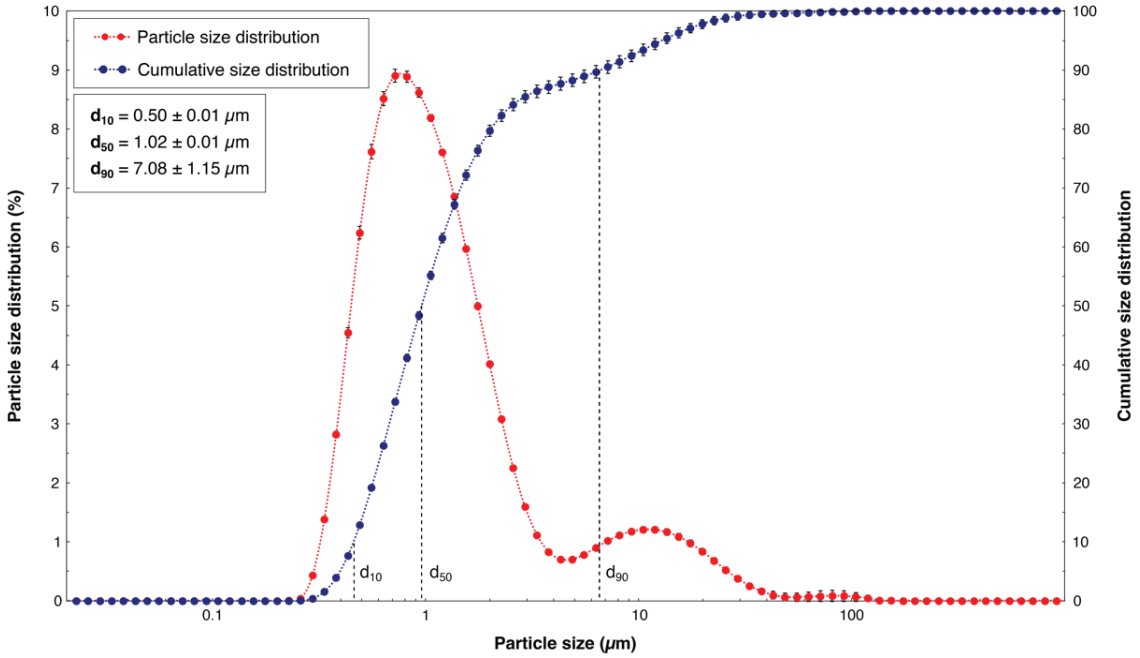

Figure 2. Particle size distribution and cumulative size distribution of the WO_3 powder used for adsorption experiments. d_{90}, d_{50}, and d_{10} are the diameters below which 90, 50 and 10% of the particles are found, respectively.

Besides, Figure 3a presents a bright-field TEM (BF-TEM) micrograph in which a few small WO_3 particles, about 200 nm and smaller, display sharp edges and a roughly rectangular shape. The actual diameter of the particles is smaller than the diameter determined by laser diffraction, possibly due to agglomeration of the particles in the aqueous phase, even when a ultrasonic treatment was applied. Figure 3b shows the high-resolution (HR) TEM micrograph and the corresponding SAED pattern in the inset, highlighting the high crystallinity of the sample. This

SAED pattern presented in the inset of Figure 3b corresponds to the monoclinic crystal structure, with a $P12_1/n_1$ space group.

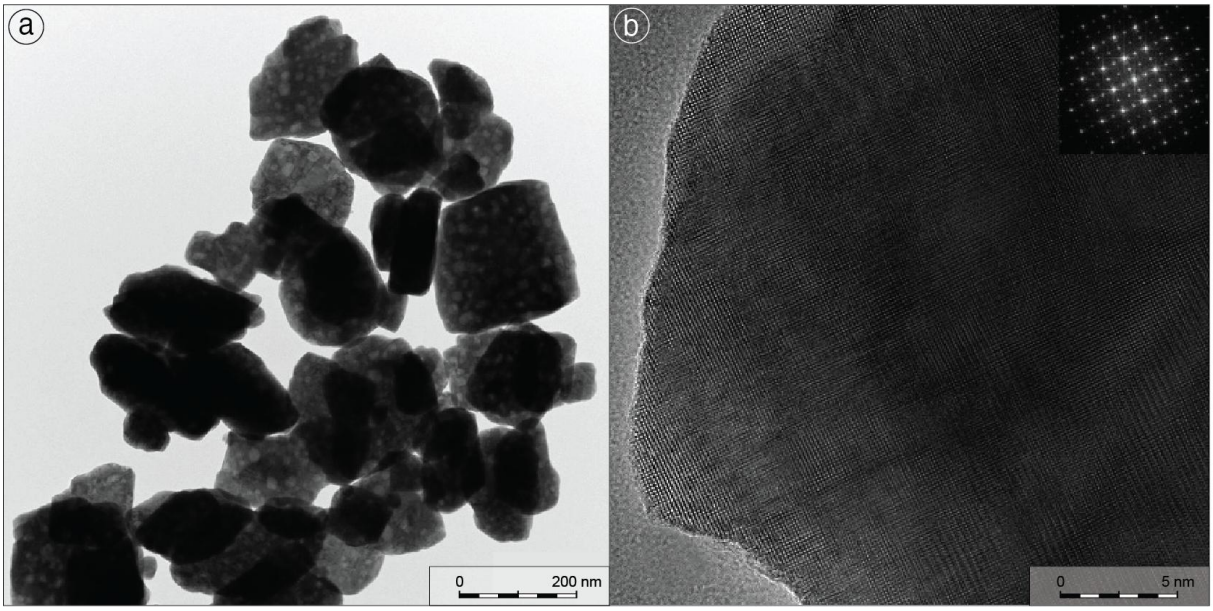

Figure 3. BF-TEM micrograph (a) and HR-TEM micrograph (b) of the synthesized WO_3 powder, with a SAED pattern in the inset.

For further characterization, the WO_3 powder was analyzed by XRD followed by Rietveld refinement using diffraction peaks of known orthorhombic and monoclinic phases of WO_3. None of these phases matched the pattern exactly, as presented in Figure S1 of the ESI. However, the fit with the monoclinic phase gave the smallest weighted profile R-factor (Rwp). The presence of the orthorhombic phase is difficult to explain as the transition temperature at which the orthorhombic phase appears is reported to be close to 603 K for bulk WO_3.[89] Nevertheless, other authors found similar results that have been attributed to defects and local distortion disorder.[90] Using single-crystal XRD, Loopstra and Rietveld reported that m-WO_3, generally synthesized by dehydration of $WO_3 \cdot H_2O$, crystallizes in a monoclinic symmetry with the space group $P2_1/n$.[91] However, Szymanski and Robert, using a similar XRD technique, indicated that it crystallizes in the orthorhombic system with the space group $Pmnb$.[92]

The N_2 isotherm measured at 77 K was perfectly reversible since adsorption and desorption branches were roughly the same (Figure S2 of the ESI). Their modelling using the BET equation resulted in a specific area of 4.2 $m^2 \cdot g^{-1}$. This value was used for the subsequent comparison between experimental and theoretical results of water adsorption on WO_3.

3.2. Experimental results of water adsorption

Adsorption isotherms

Water adsorption isotherms at 285, 295, 305 and 315 K are presented in Figure 4a, with a zoom on the low equilibrium pressure range in **Figure *4***b. The four obtained isotherms display a similar shape with three distinct zones. The amount of water adsorbed first rises significantly and, at intermediate equilibrium pressure, reaches a knee after which it increases slowly with pressure. At high equilibrium pressure, water condensation occurs on the sample as well as on the tube of the sample holder, which results in a very rapid increase in the amount of adsorbed water. The adsorption isotherms obtained are type II, which is traditionally interpreted by a high adsorption energy of the considered molecule on a non-porous material.[61] This is consistent with the crystallographic structure of WO_3, which, according to its characterization, has good crystallinity and, therefore, does not have nano- or micrometer-sized pores. Obtaining a type II isotherm is also consistent with the significantly polar nature of WO_3 surfaces, which induces a considerable affinity for water molecules (Figure 1). The type II isotherm comes from the fact that the adsorption of the first water molecules, *i.e.*, at low pressure, on the WO_3 surface occurs with a high adsorption energy, which steadily decreases when several layers are formed on the surface, until reaching water condensation.

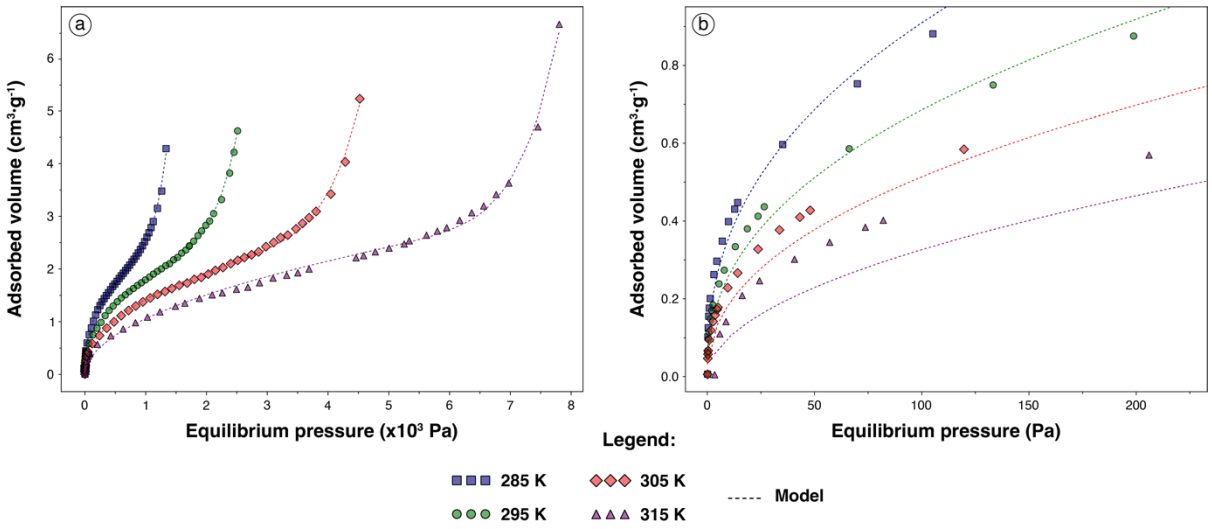

Figure 4. (a) Water vapor adsorption isotherms on WO_3 powder at 285, 295, 305, and 315 K (dots) and their fits using a Dual-Site Freundlich-Langmuir model (dashed lines); (b) Zoom into the low uptake region (0 to 0.9 $cm^3 \cdot g^{-1}$) showing the four isotherms and their fits.

Derivative isotherm summation approach

We plotted the derivative of the adsorbed volume expressed as a function of $\ln(p/p_0)$, see **Figure 5**, following the derivative isotherm summation (DIS) approach developed by Villieras and coworkers.[93] This method allows for a quantitative estimation of the surface heterogeneity as well as for an identification of the possible adsorption sites from low-pressure gas adsorption isotherms, generally performed using N_2 or Ar. It consists in fitting the derivative of the experimental isotherm with respect to $\ln(p/p_0)$ by a linear combination of derivative isotherm equations that describe adsorption on homogeneous surfaces. Considering the polarity and under-coordination of the (001) WO_3 surface, the affinity of water for this surface is large, resulting in the fact that each adsorption layer is completed before starting to form another layer. Hence, we selected the extension of the Langmuir isotherm that includes lateral interactions, the Bragg-Williams-Temkin isotherm,[94] to describe each homogeneous local isotherm.

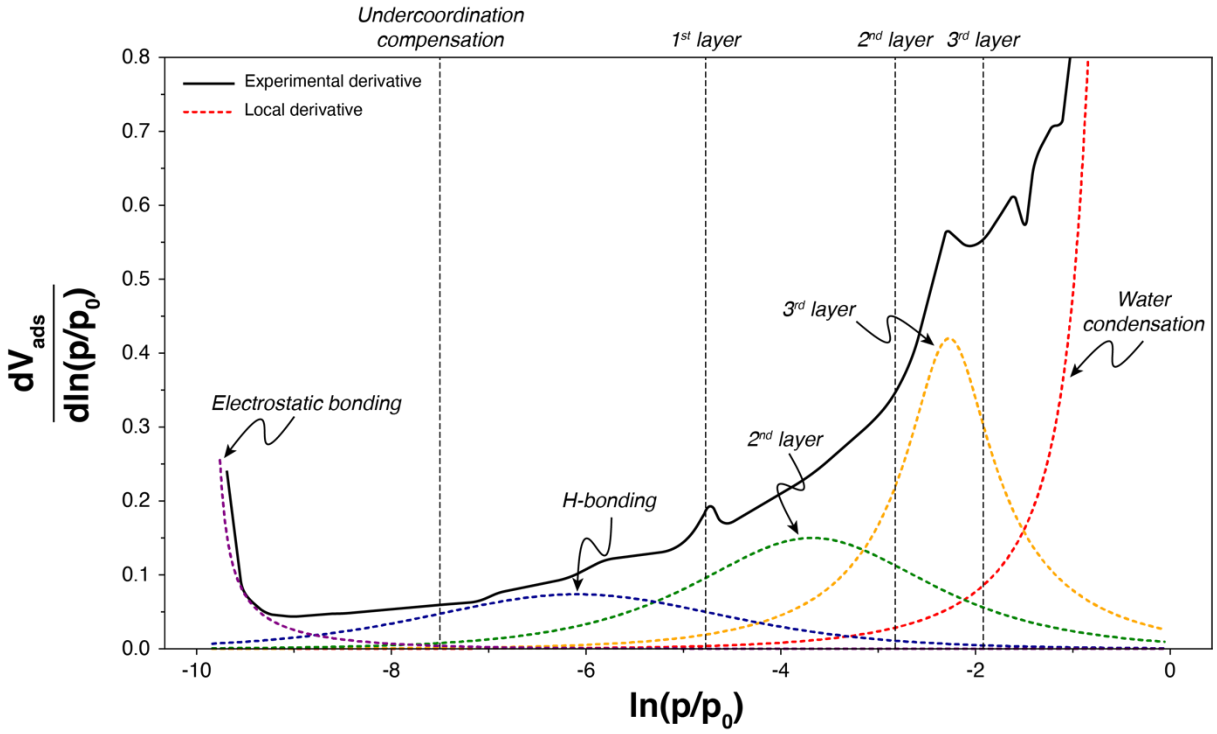

Figure 5. Derivative of the experimental adsorption isotherm of water on WO_3 at 295 K and its decomposition into five fitted local first derivates of adsorption isotherms on homogeneous surfaces (Langmuir models with lateral interactions). Each fit corresponds to a Bragg-Williams-Temkin adsorption isotherm applied to a homogeneous surface.

Given the high affinity of WO_3 surfaces for water, the equilibrium pressure was not low enough to capture the adsorption of the very first water molecules on the surface. This is highlighted by the significant decrease in the derivative when increasing $\ln(p/p_0)$ from the lowest $\ln(p/p_0)$, which can be interpreted as the end of the adsorption of water molecules on the high-affinity adsorption sites (Figure 5). On the one hand, these adsorption sites may correspond to sites located on surfaces that present higher surface energy compared to the (001) surface, which is reported to be the most stable surface for WO_3. Indeed, a significant amount of different terminations, such as the (100), (010) and (110) surfaces, may be exposed on WO_3 nanoparticles.[85,86] Since these surfaces are less stable than the (001) surface, they present higher surface energy resulting in a stronger affinity for water molecules. On the other hand, these high-affinity adsorption sites may also correspond to the under-coordinated tungsten atoms on the (001) surface. Overall, interpretations are difficult for the first adsorption sites since the experimental pressures were not

low enough to observe the complete local derivate isotherm. Then, when $\ln(p/p_0)$ is increased, another derivative isotherm describes the adsorption, without lateral interaction but with a significant energy constant, considering the value of p/p_0 at maximum (Figure 5). These second adsorption sites can be attributed to the adsorption of water molecules on the surface by means of hydrogen bonds, since all under-coordinated tungsten atoms are occupied by water molecules. At this value of coverage, based on a specific cross-sectional area of water molecule of about 0.1 nm^2, the surface is composed half of adsorbed water molecules and half of under-coordinated oxygen atoms. The water molecules probably adsorb by establishing hydrogen bonds with the under-coordinated oxygen atoms and the adsorbed water molecules, which makes the surface quite homogeneous in terms of energy. When $\ln(p/p_0)$ is further increased, two other local isotherms describe water adsorption (Figure 5) that can be interpreted as the filling of the second and third water layer on the WO_3 surface, respectively. This is followed by water condensation, *i.e.*, multilayer adsorption, which is described by another local isotherm with significant lateral interactions but a low energy constant.

Isosteric enthalpy of adsorption

The isosteric enthalpy of adsorption was calculated by applying the Clausius-Clapeyron approach either directly to the experimental data or to the DSFL models fitted to the experimental points (Figure 6). Nonetheless, as discussed above, the experimental equilibrium pressures were not low enough to observe the adsorption of the very first water molecules on the WO_3 surface. Hence, using the DSFL models, the adsorption isotherms were extrapolated to an adsorbed volume of 0.04 $cm^3 \cdot g^{-1}$, which corresponds to a surface coverage of around 1 molecule$\cdot nm^{-2}$. At this value of surface coverage, the water molecules are roughly 1 nm apart from each other and, therefore, they do not interact and can be considered isolated. For this point, the calculated isosteric enthalpy of adsorption is approximately -90 $kJ \cdot mol^{-1}$, which is consistent with the values reported for the adsorption of molecules on polar mineral surfaces.[66,95,96] The isosteric enthalpy of adsorption decreases significantly with the adsorbed volume, which corresponds to the formation of several layers (Figure 6). The second layer presents an average ΔH_{ads} between -55 $kJ \cdot mol^{-1}$ (from models) and -47 $kJ \cdot mol^{-1}$ (from experimental points) and the third layer has an average ΔH_{ads} between -50 $kJ \cdot mol^{-1}$ (from models) and -46 $kJ \cdot mol^{-1}$ (from experimental points). The enthalpy of condensation of water (around -43 $kJ \cdot mol^{-1}$ in the range of

temperatures considered here) is reached just after the completion of the third layer. Overall, the influence of the surface decreases sharply as the coverage increases and no longer has an effect after the completion of the third layer, due to the screening effect of the previous adsorbed layers. The two methods used to calculate the isosteric enthalpy of adsorption provide similar results, except for the intermediate adsorbed amounts, which correspond to the area in which the errors between the models and the experimental points are the highest (see again Figure 4).

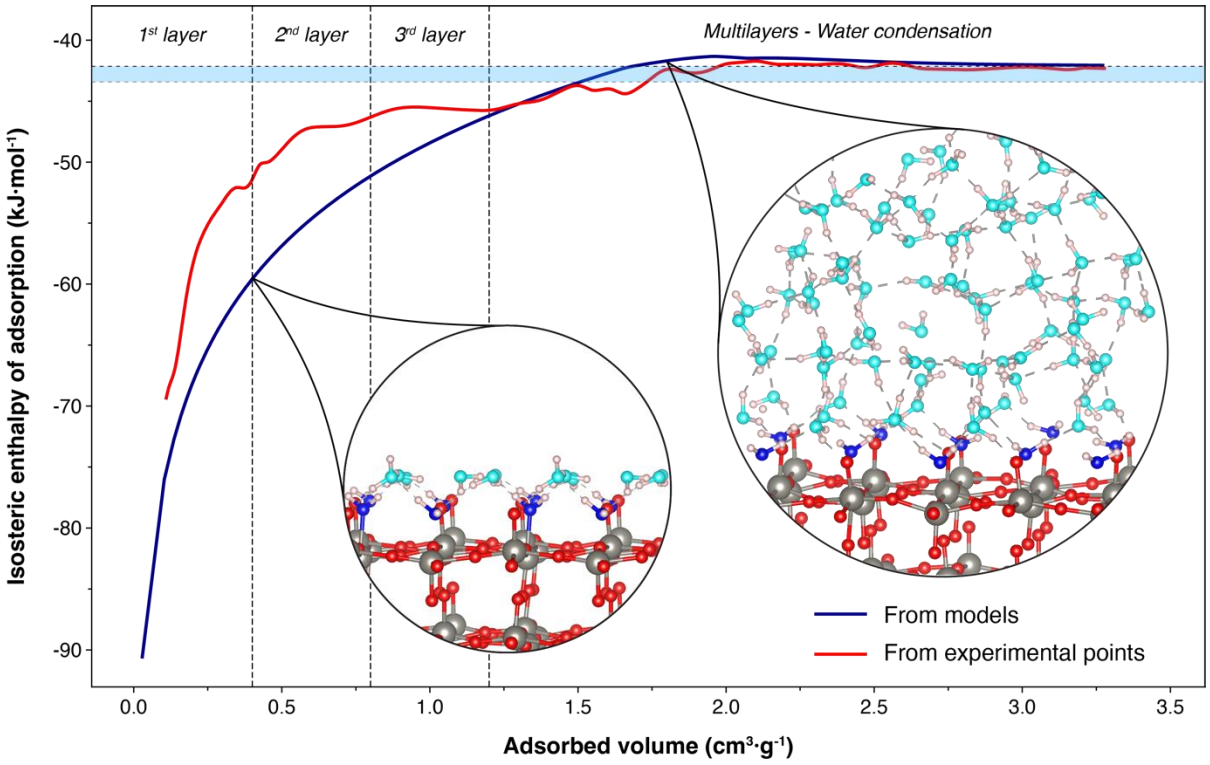

Figure 6. Isosteric enthalpy of water vapor adsorption on WO_3 as a function of the adsorbed amount, calculated directly from the experimental points (red curve) and from the DSFL models fitted to the experimental points (blue curve). The light blue zone corresponds to the enthalpy of condensation of water for the temperature range used in this work (285 – 315 K). Snapshots extracted from DFT simulations (see next section) are included to visualize the coverage increase.

3.3. Computational analysis

In the following, we discuss the results obtained by static DFT calculations and ab initio MD simulations, performed to gain further atomistic insights into the hydration mechanisms of the (001) WO_3 surface.

Progressive surface hydration at 0 K

First, we analyzed in detail the structural features and the adsorption energies of water molecules on the (001) surface for increasing values of surface coverage. As the molecular adsorption mode is known to be favored on the WO_3 surface,[41,46,55,56] the progressive hydration of the surface was investigated by considering only undissociated water molecules. Addition of the first 8 water molecules corresponds to one molecule for each under-coordinated surface tungsten atom (W_{5c}) in our surface slab. These molecules adsorbed onto the surface by establishing O_w - W_{5c} bonds (Figure 7), whose length was about 2.32 Å, and by forming hydrogen bonds with the neighboring O_t, with H_w - O_t bond lengths between 1.8 and 2.2 Å.

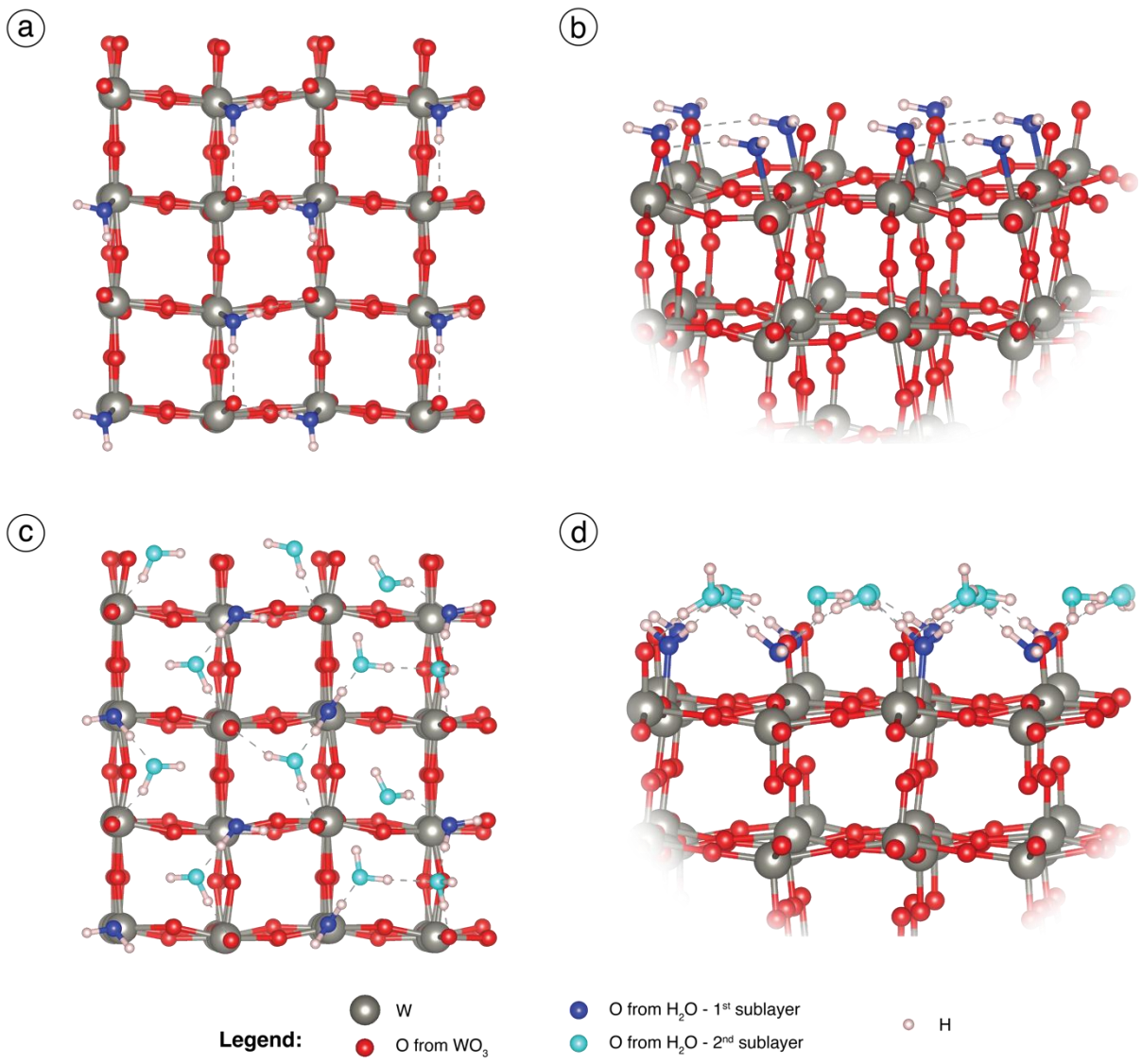

Figure 7. Top (a and c) and side (b and d) views of the first 8 water molecules (a and b) and of the first layer (c and d) of water molecules adsorbed on the (001) surface of WO_3. The first 8 water molecules (40% of the layer) correspond to coordination to the 5-coordinated W_{5c} atoms. The first layer, which comprises 20 water molecules, is defined by considering only those water molecules that establish bonds with the WO_3 surface. The dashed lines represent hydrogen bonds.

The computed isosteric adsorption energy (and dispersive energy contribution) was roughly constant for the first 8 water molecules (Figure 8a), ranging from -108.2 $kJ \cdot mol^{-1}$

(-28.5 kJ·mol^{-1}) to -102.5 kJ·mol^{-1} (-22.7 kJ·mol^{-1}). When the surface coverage was gradually increased to 20 molecules, representing a full layer, the isosteric adsorption energy of the last 12 water molecules decreased in absolute value to an average value of -64.2 kJ·mol^{-1} (Figure 8a), with an average contribution from dispersion of -13.8 kJ·mol^{-1}. The first 8 water molecules were adsorbed on the 8 surface W_{5c} atoms and compensated for their under-coordination. The remaining 12 water molecules were adsorbed by establishing hydrogen bonds with the first 8 adsorbed water molecules, with an average bond length of about 1.58 Å, but also with the 8 surface O_t atoms, with d = 1.85 Å on average (Figure 7). These 20 molecules are therefore part of the first layer since they all interacted with the surface, although the 8- and 12-molecules sub-layers could be differentiated. Some of the adsorbed water molecules also interacted with other adsorbed water molecules (d = 1.80 Å), in order to reproduce the water structuration, as it has been extensively described in the literature.[97,98]

Finally, when the water coverage was increased from 20 to 32 water molecules, the isosteric adsorption energy remained roughly constant at around -67 kJ·mol^{-1} (Figure 8a). Besides, increasing the surface coverage and the number of water layers did not affect the order and structure of the under-layers. The molecules constituting the second layer interacted with neighboring water molecules of the first and second layers through H-bonds, with bond lengths ranging from 1.63 Å to 1.92 Å. These interactions induced the structuration of the water near the surface and the creation of water clusters involving 3 to 6 water molecules. It is noteworthy that static DFT calculations overestimated the isosteric adsorption energy at low and high coverage values, compared to the experimental results (Figure 8b). Meanwhile, the inclusion of an implicit solvent decreased the isosteric adsorption energy in absolute value by between 30 and 40 kJ·mol^{-1} for all surface coverage values, although the constant trend on surface coverage remained unchanged (Figure 8a). This is in rough agreement with previous work[46] using CANDLE and SaLSA solvation models (-38.6 and -29.9 kJ·mol^{-1}, respectively). Similarly, the adsorption energies are underestimated compared to the experimental results when an implicit solvent is used (Figure 8b).

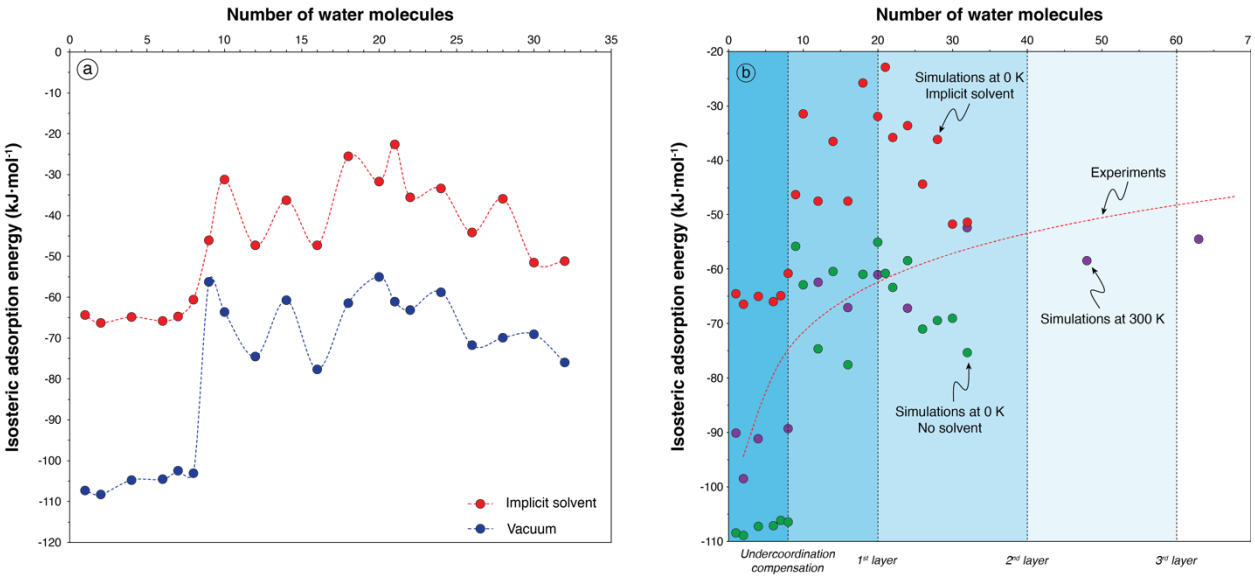

Figure 8. (a) Isosteric adsorption energy of water on the (001) surface of WO_3 as a function of water coverage, without/with inclusion of implicit solvent, determined by static DFT calculations. (b) Isosteric adsorption energy of water on the (001) surface of WO_3 from experiments (red dashed curve), DFT-MD simulations conducted at 300 K (purple circles), static DFT calculations without implicit solvent (green circles) and with implicit solvent (red circles).

Progressive surface hydration at finite temperature

To assess the effect of finite temperature on the WO_3 hydration mechanisms and on the water adsorption energies, and to improve the results obtained from static DFT calculations, we conducted DFT-MD simulations at 300 K for various values of surface coverage (Figure 8b). The energies obtained from the DFT-MD simulations can be considered as isosteric adsorption enthalpies of water and are therefore directly comparable to the experimental values. The DFT-MD simulations were performed with an increasing number of water molecules, from 1 to 64, approximately corresponding to three water layers on the surface.

First, no spontaneous dissociation of water molecules was observed on the surface, in contrast to what was observed during DFT-MD simulation of hydrated NiO surfaces by some of us,[53] confirming that water dissociation requires a rather large activation energy on the (001) WO_3 surface. Moreover, the molecular mechanisms involved in the adsorption of the water molecules were roughly the same as those predicted at 0 K. The first 8 water molecules were coordinated to

the 5-coordinated surface W_{5c} atoms with an average $O_w - W_{5c}$ bond length of 2.38 Å. The computed isosteric enthalpy of adsorption was almost constant for these 8 water molecules at around -92.3 kJ·mol^{-1}, including a contribution from dispersive interactions of -24.0 kJ·mol^{-1} (Figure 8b). Once the under-coordination of the surface W_{5c} atoms was saturated and before the first layer was completed, the computed isosteric enthalpy of adsorption decreased in absolute value to an average value of -63.5 kJ·mol^{-1} (with an average dispersion contribution of -14.1 kJ·mol^{-1}). The remaining 12 molecules in the layer formed acceptor H-bonds with the first 8 molecules beneath them and donor H-bonds with the surface O_t atoms, with average bond lengths of around 1.69 Å and 1.85 Å, respectively. When the surface coverage was further increased to two and three layers, the isosteric enthalpy of hydration decreased in absolute value to about -50 kJ·mol^{-1}. This value was close to the experimental enthalpy of condensation of water, which is about -42 kJ·mol^{-1}. This is consistent with the gradual decrease of the influence of the surface on the adsorbed water molecules. Overall, the isosteric enthalpy of adsorption of water calculated at 300 K followed the same trend as that calculated at 0 K by static DFT calculations, although, as usually observed, [95,96,99] the interaction energy was reduced due to the effect of temperature. Besides, the theoretical results obtained at 300 K by the DFT-MD simulations were in quantitative agreement with the isosteric enthalpy of adsorption calculated from the adsorption isotherms and with the DIS approach. Indeed, the first 8 water molecules considered in the DFT-MD simulations corresponded to the first molecules adsorbed on the surface, identified using the DIS approach and whose adsorption was attributed to electrostatic bonding considering the high affinity of the surface (Figure 5). In addition, the 12 following water molecules, whose adsorption by means of hydrogen bonds leads to the formation of the first complete water layer, were also identified using the DIS approach (Figure 5).

Finally, to assess the influence of the (001) WO_3 surface on the structure of the water, a DFT-MD simulation was performed, in which the cell was completely filled with water molecules (Figure 9a). In this case, the number of water molecules was chosen to obtain a water density of around 1 g·cm^{-3}. The presence of multiple water layers did not affect the geometric configuration of the first layers described at 300 K, and the same adsorption mechanisms reported above were observed. As previously shown, the adsorption of 8 water molecules per tungsten atom, forming the first sub-layer, also occurs for the full hydrated cell (Figure 9a). Also, once the under-coordinated W_{5c} surface atoms were saturated, the water molecules are adsorbed

by means of hydrogen bonds. Besides, one can observe that the water layers near the surface form a structured configuration, which is stable during the MD simulation. Overall, the structural influence of the surface on the water was limited to a few layers, as can be seen from the density profile drawn on the DFT-MD simulation (Figure 9b). In Figure 9b, the significant peak in zone I corresponds to the first sub-layer of the first layer, *i.e.*, the molecules electrostatically bonded to the under-coordinated surface tungsten atoms, while zone I' corresponds to the water molecules adsorbed by means of hydrogen bonds, leading to the formation of the first adsorption layer. Then, zone II represents the second adsorption layer, in which the molecules are exclusively adsorbed by means of hydrogen bonds, while zone III corresponds to multiple adsorption layers. It is noteworthy that the third layer is very similar to the next layers since the density for the third layer is not higher than the density for the other layers. The other multiple layers, identified by the density peak they form, correspond to bulk water, in which density oscillations are common due to the layered structuration of water.[100–102] Hence, the influence of the (001) WO_3 surface on the water structure was limited to two layers, which is consistent with the isosteric enthalpy of hydration.

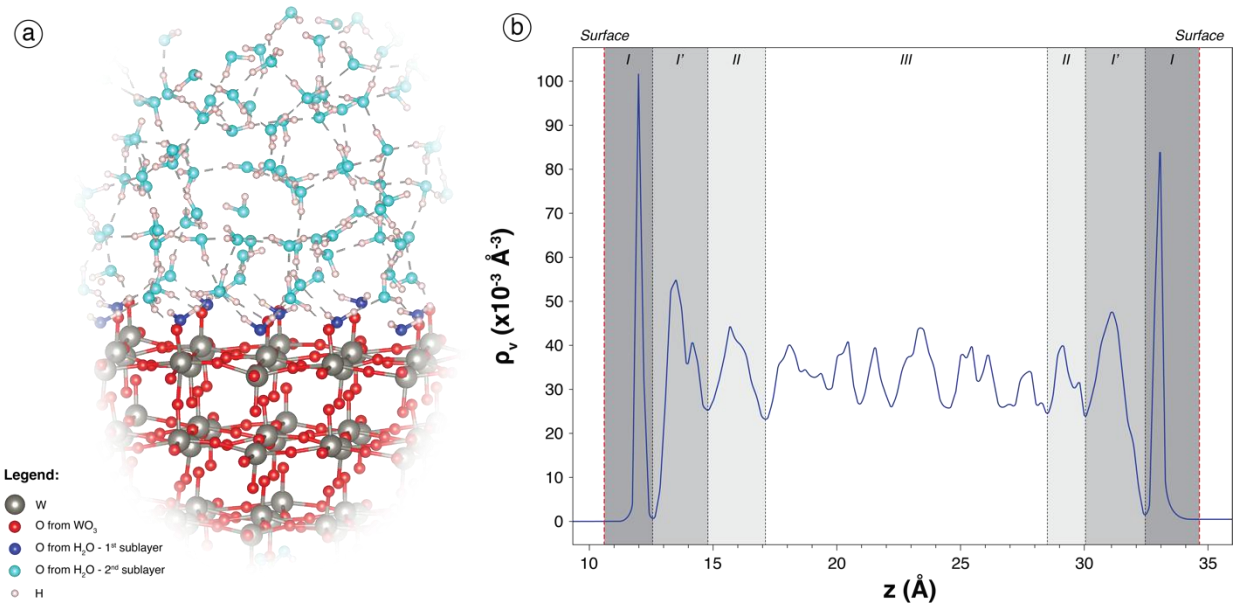

Figure 9. (a) Snapshot of a side view of the (001) WO_3 surface above which the space has been completely filled with water molecules. The dashed lines represent hydrogen bonds. Lone atoms and repeated boundaries are due to the periodicity of the cell. (b) Number density profile of

water molecules along the water slab in contact with the (001) WO_3 surface (red dashed lines). Zones I, I', II, and III correspond to the first sub-layer of the first layer, the second sub-layer of the first layer, the second layer, and multiple layers (water bulk), respectively.

4. Conclusions

In this work, we investigated the hydration mechanisms of the (001) surface of WO_3, using adsorption experiments combined with static DFT calculations and DFT-MD simulations. First, we demonstrated that static DFT calculations tend to overestimate, in absolute value, the calculated isosteric enthalpy of adsorption compared to the experimental results. The inclusion of an implicit solvent in the simulations, to account for the surrounding water, leads to the decrease of the absolute value of the isosteric enthalpy of adsorption and, therefore, to an underestimation of the isosteric enthalpy of adsorption compared to the experimental results. Second, we have shown, based on DFT-MD simulations – which account for finite temperature effects – that the first water molecules adsorb in molecular form by bonding to the under-coordinated surface tungsten atoms with $\Delta H_{ads} \approx$ -92.3 kJ·mol^{-1} at 300 K; these results are in quantitative agreement with the value of -90 kJ·mol^{-1} calculated from experiments. When the coverage is increased, water molecules adsorb by establishing hydrogen bonds with the first adsorbed molecules and the under-coordinated surface oxygen atoms. The isosteric enthalpy of adsorption decreases in absolute value, which is consistent with the experimental results, and tends towards the enthalpy of condensation of water when the coverage increases further. The influence of the WO_3 surface on water molecules is limited to a few adsorption layers, although the structuration of water near the surface is significant. Overall, we demonstrated at the atomistic scale the high stability of hydrated WO_3 surfaces and their high affinity for water. We have built and validated a comprehensive hydration model that we share with the community and that can be used in the future for theoretical studies of (photo)catalytic mechanisms involving WO_3.

ASSOCIATED CONTENT

Electronic Supplementary Information

(Add the description of the experimental graphs S1 and S2); Calculated adsorption energies in vacuum (including implicit solvent), dispersion energies and isosteric adsorption energies, at 0 K, as a function of explicit water coverage; The internal coordinates of the full hydrated WO_3 model (PDF)

The supporting information is available free of charge.

AUTHOR INFORMATION

Corresponding authors

Yann Foucaud – *Université de Lorraine & CNRS, LPCT, UMR 7019, F-54000 Nancy, France ;* Email : yann.foucaud@univ-lorraine.fr

Michael Badawi – *Université de Lorraine & CNRS, LPCT, UMR 7019, F-54000 Nancy, France ;* Email : michael.badawi@univ-lorraine.fr

Mariachiara Pastore – *Université de Lorraine & CNRS, LPCT, UMR 7019, F-54000 Nancy, France ;* Email :mariachiara.pastore@univ-lorraine.fr

Authors

Azza Ben Jannet – *Université de Lorraine & CNRS, LPCT, UMR 7019, F-54000 Nancy, France ; Université de Monastir, FSM, LMCN, LR11ES40, 5000 Monastir, Tunisie*

Stefano Caramori – *Dipartimento di Scienze Chimiche, Farmaceutiche ed Agrarie, 44121 Ferrara, Italy*

Rafael Canevesi – *Université de Lorraine & CNRS, Institut Jean Lamour (IJL), F-88000 Épinal, France*

Moncef Said – *Université de Monastir, FSM, LMCN, LR11ES40, 5000 Monastir, Tunisie*

Alain Celzard – *Université de Lorraine & CNRS, Institut Jean Lamour (IJL), F-88000 Épinal, France ; Institut Universitaire de France (IUF)*

Vanessa Fierro – *Université de Lorraine & CNRS, Institut Jean Lamour (IJL), F-88000 Épinal, France*

Notes

The authors declare no competing financial interest.

ACKNOWLEDGMENTS

Y.F., M.P. and M.B. are grateful for the financial support given by the COMETE project (COnception in silico de Matériaux pour l'EnvironnemenT et l'Energie), co-funded by the European Union as part of the "FEDER-FSE Lorraine et Massif des Vosges 2014−2020" program. This work benefited from access to the HPC resources of TGCC under the allocations 2021-A0100810433 and 2022-A0120810433 by GENCI –EDARI project. Computational resources were also provided by the EXPLOR mesocenter of the Université de Lorraine (project 2018CPMXX0602).

REFERENCES

(1) Fujishima, A.; Honda, K. Electrochemical Photolysis of Water at a Semiconductor Electrode. *Nature* **1972**, *238* (5358), 37–38. https://doi.org/10.1038/238037a0.

(2) Liu, G.; Sheng, Y.; Ager, J. W.; Kraft, M.; Xu, R. Research Advances towards Large-Scale Solar Hydrogen Production from Water. *EnergyChem* **2019**, *1* (2), 100014. https://doi.org/10.1016/j.enchem.2019.100014.

(3) Nishiyama, H.; Yamada, T.; Nakabayashi, M.; Maehara, Y.; Yamaguchi, M.; Kuromiya, Y.; Nagatsuma, Y.; Tokudome, H.; Akiyama, S.; Watanabe, T.; Narushima, R.; Okunaka, S.; Shibata, N.; Takata, T.; Hisatomi, T.; Domen, K. Photocatalytic Solar Hydrogen Production from Water on a 100-M2 Scale. *Nature* **2021**, *598* (7880), 304–307. https://doi.org/10.1038/s41586-021-03907-3.

(4) Hisatomi, T.; Domen, K. Reaction Systems for Solar Hydrogen Production via Water Splitting with Particulate Semiconductor Photocatalysts. *Nat. Catal.* **2019**, *2* (5), 387–399. https://doi.org/10.1038/s41929-019-0242-6.

(5) Guo, Q.; Zhou, C.; Ma, Z.; Yang, X. Fundamentals of TiO_2 Photocatalysis: Concepts, Mechanisms, and Challenges. *Adv. Mater.* **2019**, *31* (50), 1901997.

https://doi.org/10.1002/adma.201901997.

(6) Ran, J.; Zhang, J.; Yu, J.; Jaroniec, M.; Qiao, S. Z. Earth-Abundant Cocatalysts for Semiconductor-Based Photocatalytic Water Splitting. *Chem. Soc. Rev.* **2014**, *43* (22), 7787–7812. https://doi.org/10.1039/C3CS60425J.

(7) Anik, M.; Cansizoglu, T. Dissolution Kinetics of WO_3 in Acidic Solutions. *J. Appl. Electrochem.* **2006**, *36* (5), 603–608. https://doi.org/10.1007/s10800-006-9113-3.

(8) Zhang, T.; Zhu, Z.; Chen, H.; Bai, Y.; Xiao, S.; Zheng, X.; Xue, Q.; Yang, S. Iron-Doping-Enhanced Photoelectrochemical Water Splitting Performance of Nanostructured WO_3: A Combined Experimental and Theoretical Study. *Nanoscale* **2015**, *7* (7), 2933–2940. https://doi.org/10.1039/C4NR07024K.

(9) Liu, X.; Wang, F.; Wang, Q. Nanostructure-Based WO_3 Photoanodes for Photoelectrochemical Water Splitting. *Phys. Chem. Chem. Phys.* **2012**, *14* (22), 7894. https://doi.org/10.1039/c2cp40976c.

(10) Song-Can, W.; Feng-Qiu, T.; Lian-Zhou, W. Visible Light Responsive Metal Oxide Photoanodes for Photoelectrochemical Water Splitting: A Comprehensive Review on Rational Materials Design. *J. Inorg. Mater.* **2018**, *33* (2), 173. https://doi.org/10.15541/jim20170352.

(11) Tong, H.; Jiang, Y.; Zhang, Q.; Li, J.; Jiang, W.; Zhang, D.; Li, N.; Xia, L. Enhanced Interfacial Charge Transfer on a Tungsten Trioxide Photoanode with Immobilized Molecular Iridium Catalyst. *ChemSusChem* **2017**, *10* (16), 3268–3275. https://doi.org/10.1002/cssc.201700721.

(12) Sachs, M.; Park, J.-S.; Pastor, E.; Kafizas, A.; Wilson, A. A.; Francàs, L.; Gul, S.; Ling, M.; Blackman, C.; Yano, J.; Walsh, A.; Durrant, J. R. Effect of Oxygen Deficiency on the Excited State Kinetics of WO_3 and Implications for Photocatalysis. *Chem. Sci.* **2019**, *10* (22), 5667–5677. https://doi.org/10.1039/C9SC00693A.

(13) Paik, T.; Cargnello, M.; Gordon, T. R.; Zhang, S.; Yun, H.; Lee, J. D.; Woo, H. Y.; Oh, S. J.; Kagan, C. R.; Fornasiero, P.; Murray, C. B. Photocatalytic Hydrogen Evolution from Substoichiometric Colloidal WO_{3-x} Nanowires. *ACS Energy Lett.* **2018**, *3* (8), 1904–1910. https://doi.org/10.1021/acsenergylett.8b00925.

(14) Di Liberto, G.; Tosoni, S.; Pacchioni, G. Theoretical Treatment of Semiconductor

Heterojunctions for Photocatalysis: The WO_3 /$BiVO_4$ Interface. *J. Phys. Condens. Matter* **2019**, *31* (43), 434001. https://doi.org/10.1088/1361-648X/ab2fa4.

(15) Zheng, G.; Wang, J.; Liu, H.; Murugadoss, V.; Zu, G.; Che, H.; Lai, C.; Li, H.; Ding, T.; Gao, Q.; Guo, Z. Tungsten Oxide Nanostructures and Nanocomposites for Photoelectrochemical Water Splitting. *Nanoscale* **2019**, *11* (41), 18968–18994. https://doi.org/10.1039/C9NR03474A.

(16) Deb, S. K. Opportunities and Challenges in Science and Technology of WO_3 for Electrochromic and Related Applications. *Sol. Energy Mater. Sol. Cells* **2008**, *92* (2), 245–258. https://doi.org/10.1016/j.solmat.2007.01.026.

(17) Granqvist, C. G. Electrochromic Tungsten Oxide films: Review of Progress 1993-1998. *Sol. Energy Mater.* **2000**, *60* (3), 201-262. https://doi.org/10.1016/S0927-0248(99)00088-4.

(18) Solis, J. L.; Saukko, S.; Kish, L.; Granqvist, C. G.; Lantto, V. Semiconductor Gas Sensors Based on Nanostructured Tungsten Oxide. *Thin Solid Films* **2001**, *391* (2), 255–260. https://doi.org/10.1016/S0040-6090(01)00991-9.

(19) Jin, H.; Zhou, H.; Zhang, Y. Insight into the Mechanism of CO Oxidation on WO_3(001) Surfaces for Gas Sensing: A DFT Study. *Sensors* **2017**, *17* (8), 1898. https://doi.org/10.3390/s17081898.

(20) Xiang, Q.; Meng, G. F.; Zhao, H. B.; Zhang, Y.; Li, H.; Ma, W. J.; Xu, J. Q. Au Nanoparticle Modified WO_3 Nanorods with Their Enhanced Properties for Photocatalysis and Gas Sensing. *J. Phys. Chem. C* **2010**, *114* (5), 2049–2055. https://doi.org/10.1021/jp909742d.

(21) Hodes, G.; Cahen, D.; Manassen, J. Tungsten Trioxide as a Photoanode for a Photoelectrochemical Cell (PEC). *Nature* **1976**, *260* (5549), 312–313. https://doi.org/10.1038/260312a0.

(22) Hümmelgen, I. A. Oxide Semiconductors for Solar Energy Conversion—Titanium Dioxide. *J. Solid State Electrochem.* **2012**, *16* (6), 2287–2287. https://doi.org/10.1007/s10008-012-1650-6.

(23) Tanaka, A.; Hashimoto, K.; Kominami, H. Visible-Light-Induced Hydrogen and Oxygen Formation over Pt/Au/WO_3 Photocatalyst Utilizing Two Types of Photoabsorption Due to Surface Plasmon Resonance and Band-Gap Excitation. *J. Am. Chem. Soc.* **2014**, *136* (2), 586–589. https://doi.org/10.1021/ja410230u.

(24) Mi, Q.; Ping, Y.; Li, Y.; Cao, B.; Brunschwig, B. S.; Khalifah, P. G.; Galli, G. A.; Gray, H. B.; Lewis, N. S. Thermally Stable N_2 -Intercalated WO_3 Photoanodes for Water Oxidation. *J. Am. Chem. Soc.* **2012**, *134* (44), 18318–18324. https://doi.org/10.1021/ja3067622.

(25) Grätzel, M. Photoelectrochemical Cells. *Nature* **2001**, *414* (6861), 338–344. https://doi.org/10.1038/35104607.

(26) Dutta, V.; Sharma, S.; Raizada, P.; Thakur, V. K.; Khan, A. A. P.; Saini, V.; Asiri, A. M.; Singh, P. An Overview on WO_3 Based Photocatalyst for Environmental Remediation. *J. Environ. Chem. Eng.* **2021**, *9* (1), 105018. https://doi.org/10.1016/j.jece.2020.105018.

(27) Kalanur, S. S.; Duy, L. T.; Seo, H. Recent Progress in Photoelectrochemical Water Splitting Activity of WO_3 Photoanodes. *Top. Catal.* **2018**, *61* (9–11), 1043–1076. https://doi.org/10.1007/s11244-018-0950-1.

(28) Adhikari, S.; Murmu, M.; Kim, D. Core- Shell Engineered WO_3 Architectures: Recent Advances from Design to Applications. *Small* **2022**, *18* (30), 2202654. https://doi.org/10.1002/smll.202202654.

(29) Murillo-Sierra, J. C.; Hernández-Ramírez, A.; Hinojosa-Reyes, L.; Guzmán-Mar, J. L. A Review on the Development of Visible Light-Responsive WO_3-Based Photocatalysts for Environmental Applications. *Chem. Eng. J. Adv.* **2021**, *5*, 100070. https://doi.org/10.1016/j.ceja.2020.100070.

(30) Diez-Cabanes, V.; Morales-García, Á.; Illas, F.; Pastore, M. Tuning the Interfacial Energetics in WO_3/WO_3 and WO_3/TiO_2 Heterojunctions by Nanostructure Morphological Engineering. *J. Phys. Chem. Lett.* **2021**, *12* (47), 11528–11533. https://doi.org/10.1021/acs.jpclett.1c03227.

(31) Diez-Cabanes, V.; Morales-García, Á.; Illas, F.; Pastore, M. Understanding the Structural and Electronic Properties of Photoactive Tungsten Oxide Nanoparticles from Density Functional Theory and *GW* Approaches. *J. Chem. Theory Comput.* **2021**, *17* (6), 3462–3470. https://doi.org/10.1021/acs.jctc.1c00293.

(32) Diez-Cabanes, V.; Pastore, M. Morphological Engineering of Inorganic Semiconductor VIS-Light-Driven Nanocatalysts: Experimental and Theoretical Understandings. *J. Phys. Chem. C* **2021**, *125* (28), 15125–15133. https://doi.org/10.1021/acs.jpcc.1c04487.

(33) Ben Jannet, A.; Said, M.; Badawi, M.; Pastore, M. First-Principles Modeling of Dye Anchoring on (001) γ-Monoclinic WO_3 Surfaces: The Role of Oxygen Vacancies. *J. Phys. Chem. C* **2022**, *126* (12), 5424–5434. https://doi.org/10.1021/acs.jpcc.1c10397.

(34) Chatten, R.; Chadwick, A. V.; Rougier, A.; Lindan, P. J. D. The Oxygen Vacancy in Crystal Phases of WO_3. *J. Phys. Chem. B* **2005**, *109* (8), 3146–3156. https://doi.org/10.1021/jp045655r.

(35) Wang, F.; Di Valentin, C.; Pacchioni, G. DFT Study of Hydrogen Adsorption On the Monoclinic WO_3 (001) Surface. *J. Phys. Chem. C* **2012**, *116* (19), 10672–10679. https://doi.org/10.1021/jp302210y.

(36) Wang, F.; Di Valentin, C.; Pacchioni, G. Electronic and Structural Properties of WO_3: A Systematic Hybrid DFT Study. *J. Phys. Chem. C* **2011**, *115* (16), 8345–8353. https://doi.org/10.1021/jp201057m.

(37) Ping, Y.; Rocca, D.; Galli, G. Electronic Excitations in Light Absorbers for Photoelectrochemical Energy Conversion: First Principles Calculations Based on Many Body Perturbation Theory. *Chem. Soc. Rev.* **2013**, *42* (6), 2437. https://doi.org/10.1039/c3cs00007a.

(38) Migas, D. B.; Shaposhnikov, V. L.; Rodin, V. N.; Borisenko, V. E. Tungsten Oxides. I. Effects of Oxygen Vacancies and Doping on Electronic and Optical Properties of Different Phases of WO_3. *J. Appl. Phys.* **2010**, *108* (9), 093713. https://doi.org/10.1063/1.3505688.

(39) Bhatt, M. D.; Lee, J. S. Recent Theoretical Progress in the Development of Photoanode Materials for Solar Water Splitting Photoelectrochemical Cells. *J. Mater. Chem. A* **2015**, *3* (20), 10632–10659. https://doi.org/10.1039/C5TA00257E.

(40) Diez-Cabanes, V.; Segalina, A.; Pastore, M. Effects of Size and Morphology on the Excited-State Properties of Nanoscale WO_3 Materials from First-Principles Calculations: Implications for Optoelectronic Devices. *ACS Appl. Nano Mater.* **2022**, *5* (11), 16289-16297. https://doi.org/10.1021/acsanm.2c03331.

(41) Albanese, E.; Di Valentin, C.; Pacchioni, G. H_2O Adsorption on WO_3 and WO_{3-x} (001) Surfaces. *ACS Appl. Mater. Interfaces* **2017**, *9* (27), 23212–23221. https://doi.org/10.1021/acsami.7b06139.

(42) Zhao, Y.; Yan, X.; Yang, K. R.; Cao, S.; Dong, Q.; Thorne, J. E.; Materna, K. L.; Zhu,

S.; Pan, X.; Flytzani-Stephanopoulos, M.; Brudvig, G. W.; Batista, V. S.; Wang, D. End-On Bound Iridium Dinuclear Heterogeneous Catalysts on WO_3 for Solar Water Oxidation. *ACS Cent. Sci.* **2018**, *4* (9), 1166–1172. https://doi.org/10.1021/acscentsci.8b00335.

(43) Teusch, T.; Klüner, T. Understanding the Water Splitting Mechanism on WO_3 (001)—A Theoretical Approach. *J. Phys. Chem. C* **2019**, *123* (46), 28233–28240. https://doi.org/10.1021/acs.jpcc.9b08268.

(44) Kishore, R.; Cao, X.; Zhang, X.; Bieberle-Hütter, A. Electrochemical Water Oxidation on WO_3 Surfaces: A Density Functional Theory Study. *Catal. Today* **2019**, *321–322*, 94–99. https://doi.org/10.1016/j.cattod.2018.02.030.

(45) Gerosa, M.; Gygi, F.; Govoni, M.; Galli, G. The Role of Defects and Excess Surface Charges at Finite Temperature for Optimizing Oxide Photoabsorbers. *Nat. Mater.* **2018**, *17* (12), 1122–1127. https://doi.org/10.1038/s41563-018-0192-4.

(46) Ping, Y.; Sundararaman, R.; Goddard III, W. A. Solvation Effects on the Band Edge Positions of Photocatalysts from First Principles. *Phys. Chem. Chem. Phys.* **2015**, *17* (45), 30499–30509. https://doi.org/10.1039/C5CP05740J.

(47) Ping, Y.; Goddard, W. A.; Galli, G. A. Energetics and Solvation Effects at the Photoanode/Catalyst Interface: Ohmic Contact versus Schottky Barrier. *J. Am. Chem. Soc.* **2015**, *137* (16), 5264–5267. https://doi.org/10.1021/jacs.5b00798.

(48) Karmodak, N.; Andreussi, O. Catalytic Activity and Stability of Two-Dimensional Materials for the Hydrogen Evolution Reaction. *ACS Energy Lett.* **2020**, *5* (3), 885–891. https://doi.org/10.1021/acsenergylett.9b02689.

(49) Pham, T. A.; Ping, Y.; Galli, G. Modelling Heterogeneous Interfaces for Solar Water Splitting. *Nat. Mater.* **2017**, *16* (4), 401–408. https://doi.org/10.1038/nmat4803.

(50) Schienbein, P.; Blumberger, J. Nanosecond Solvation Dynamics of the Hematite/Liquid Water Interface at Hybrid DFT Accuracy Using Committee Neural Network Potentials. *Phys. Chem. Chem. Phys.* **2022**, *24* (25), 15365–15375. https://doi.org/10.1039/D2CP01708C.

(51) Ulman, K.; Poli, E.; Seriani, N.; Piccinin, S.; Gebauer, R. Understanding the Electrochemical Double Layer at the Hematite/Water Interface: A First Principles Molecular Dynamics Study. *J. Chem. Phys.* **2019**, *150* (4), 041707. https://doi.org/10.1063/1.5047930.

(52) Mu, R.; Zhao, Z.; Dohnálek, Z.; Gong, J. Structural Motifs of Water on Metal Oxide Surfaces. *Chem. Soc. Rev.* **2017**, *46* (7), 1785–1806. https://doi.org/10.1039/C6CS00864J.

(53) Segalina, A.; Lebègue, S.; Rocca, D.; Piccinin, S.; Pastore, M. Structure and Energetics of Dye-Sensitized NiO Interfaces in Water from Ab Initio MD and Large-Scale GW Calculations. *J. Chem. Theory Comput.* **2021**, *17* (8), 5225–5238. https://doi.org/10.1021/acs.jctc.1c00354.

(54) Piccinin, S.; Rocca, D.; Pastore, M. Role of Solvent in the Energy Level Alignment of Dye-Sensitized NiO Interfaces. *J. Phys. Chem. C* **2017**, *121* (40), 22286–22294. https://doi.org/10.1021/acs.jpcc.7b08463.

(55) Hurtado-Aular, O.; Vidal, A. B.; Sierraalta, A.; Añez, R. Periodic DFT Study of Water Adsorption on m-WO_3(001), m-WO_3(100), h-WO_3(001) and h-WO_3(100). Role of Hydroxyl Groups on the Stability of Polar Hexagonal Surfaces. *Surf. Sci.* **2020**, *694*, 121558. https://doi.org/10.1016/j.susc.2019.121558.

(56) Zhang, L.; Wen, B.; Zhu, Y.-N.; Chai, Z.; Chen, X.; Chen, M. First-Principles Calculations of Water Adsorption on Perfect and Defect WO_3(0 0 1). *Comput. Mater. Sci.* **2018**, *150*, 484–490. https://doi.org/10.1016/j.commatsci.2018.04.056.

(57) Staerz, A.; Kobald, A.; Russ, T.; Weimar, U.; Hémeryck, A.; Barsan, N. Thermal Water Splitting on the WO_3 Surface: Experimental Proof. *ACS Appl. Electron. Mater.* **2020**, *2* (10), 3254–3262. https://doi.org/10.1021/acsaelm.0c00577.

(58) Staerz, A.; Berthold, C.; Russ, T.; Wicker, S.; Weimar, U.; Barsan, N. The Oxidizing Effect of Humidity on WO_3 Based Sensors. *Sens. Actuators B Chem.* **2016**, *237*, 54–58. https://doi.org/10.1016/j.snb.2016.06.072.

(59) Staerz, A.; Somacescu, S.; Epifani, M.; Kida, T.; Weimar, U.; Barsan, N. WO_3-Based Gas Sensors: Identifying Inherent Qualities and Understanding the Sensing Mechanism. *ACS Sens.* **2020**, *5* (6), 1624–1633. https://doi.org/10.1021/acssensors.0c00113.

(60) Pokhrel, S.; Simion, C. E.; Teodorescu, V. S.; Barsan, N.; Weimar, U. Synthesis, Mechanism, and Gas-Sensing Application of Surfactant Tailored Tungsten Oxide Nanostructures. *Adv. Funct. Mater.* **2009**, *19* (11), 1767–1774. https://doi.org/10.1002/adfm.200801171.

(61) Thommes, M.; Kaneko, K.; Neimark, A. V.; Olivier, J. P.; Rodriguez-Reinoso, F.; Rouquerol, J.; Sing, K. S. W. Physisorption of Gases, with Special Reference to the Evaluation of Surface Area and Pore Size Distribution (IUPAC Technical Report). *Pure Appl. Chem.* **2015**, *87* (9–10), 1051–1069. https://doi.org/10.1515/pac-2014-1117.

(62) Sircar, S.; Cao, D. V. Heat of Adsorption. *Chem. Eng. Technol.* **2002**, *25* (10), 945–948. https://doi.org/10.1002/1521-4125(20021008)25:10<945::AID-CEAT945>3.0.CO;2-F.

(63) Nuhnen, A.; Janiak, C. A Practical Guide to Calculate the Isosteric Heat/Enthalpy of Adsorption *via* Adsorption Isotherms in Metal–Organic Frameworks, MOFs. *Dalton Trans.* **2020**, *49* (30), 10295–10307. https://doi.org/10.1039/D0DT01784A.

(64) Langmuir, I. The Adsorption of Gases on Plane Surfaces of Glass, Mica and Platinum. *J. Am. Chem. Soc.* **1918**, *40* (9), 1361–1403. https://doi.org/10.1021/ja02242a004.

(65) Freundlich, H. Über Die Adsorption in Lösungen. *Z. Für Phys. Chem.* **1907**, *57U* (1), 385–470. https://doi.org/10.1515/zpch-1907-5723.

(66) Foucaud, Y.; Canevesi, R. L. S.; Celzard, A.; Fierro, V.; Badawi, M. Hydration Mechanisms of Scheelite from Adsorption Isotherms and Ab Initio Molecular Dynamics Simulations. *Appl. Surf. Sci.* **2021**, *562*, 150137. https://doi.org/10.1016/j.apsusc.2021.150137.

(67) Levenberg, K. A Method for the Solution of Certain Non-Linear Problems in Least Squares. *Q. Appl. Math.* **1944**, *2* (2), 164–168. https://doi.org/10.1090/qam/10666.

(68) Marquardt, D. W. An Algorithm for Least-Squares Estimation of Nonlinear Parameters. *J. Soc. Ind. Appl. Math.* **1963**, *11* (2), 431–441. https://doi.org/10.1137/0111030.

(69) Virtanen, P.; Gommers, R.; Oliphant, T. E.; Haberland, M.; Reddy, T.; Cournapeau, D.; Burovski, E.; Peterson, P.; Weckesser, W.; Bright, J.; van der Walt, S. J.; Brett, M.; Wilson, J.; Millman, K. J.; Mayorov, N.; Nelson, A. R. J.; Jones, E.; Kern, R.; Larson, E.; Carey, C. J.; Polat, İ.; Feng, Y.; Moore, E. W.; VanderPlas, J.; Laxalde, D.; Perktold, J.; Cimrman, R.; Henriksen, I.; Quintero, E. A.; Harris, C. R.; Archibald, A. M.; Ribeiro, A. H.; Pedregosa, F.; van Mulbregt, P.; SciPy 1.0 Contributors; Vijaykumar, A.; Bardelli, A. P.; Rothberg, A.; Hilboll, A.; Kloeckner, A.; Scopatz, A.; Lee, A.; Rokem, A.; Woods, C. N.; Fulton, C.; Masson, C.; Häggström, C.; Fitzgerald, C.; Nicholson, D. A.; Hagen, D. R.; Pasechnik, D. V.; Olivetti, E.; Martin, E.; Wieser, E.; Silva, F.; Lenders, F.; Wilhelm, F.; Young, G.; Price, G. A.; Ingold, G.-

L.; Allen, G. E.; Lee, G. R.; Audren, H.; Probst, I.; Dietrich, J. P.; Silterra, J.; Webber, J. T.; Slavič, J.; Nothman, J.; Buchner, J.; Kulick, J.; Schönberger, J. L.; de Miranda Cardoso, J. V.; Reimer, J.; Harrington, J.; Rodríguez, J. L. C.; Nunez-Iglesias, J.; Kuczynski, J.; Tritz, K.; Thoma, M.; Newville, M.; Kümmerer, M.; Bolingbroke, M.; Tartre, M.; Pak, M.; Smith, N. J.; Nowaczyk, N.; Shebanov, N.; Pavlyk, O.; Brodtkorb, P. A.; Lee, P.; McGibbon, R. T.; Feldbauer, R.; Lewis, S.; Tygier, S.; Sievert, S.; Vigna, S.; Peterson, S.; More, S.; Pudlik, T.; Oshima, T.; Pingel, T. J.; Robitaille, T. P.; Spura, T.; Jones, T. R.; Cera, T.; Leslie, T.; Zito, T.; Krauss, T.; Upadhyay, U.; Halchenko, Y. O.; Vázquez-Baeza, Y. SciPy 1.0: Fundamental Algorithms for Scientific Computing in Python. *Nat. Methods* **2020**, *17* (3), 261–272. https://doi.org/10.1038/s41592-019-0686-2.

(70) Kresse, G.; Hafner, J. Ab Initio Molecular Dynamics for Liquid Metals. *Phys. Rev. B* **1993**, *47* (1), 558–561. https://doi.org/10.1103/PhysRevB.47.558.

(71) Blöchl, P. E. Projector Augmented-Wave Method. *Phys. Rev. B* **1994**, *50* (24), 17953–17979. https://doi.org/10.1103/PhysRevB.50.17953.

(72) Kresse, G.; Joubert, D. From Ultrasoft Pseudopotentials to the Projector Augmented-Wave Method. *Phys. Rev. B* **1999**, *59* (3), 1758–1775. https://doi.org/10.1103/PhysRevB.59.1758.

(73) Perdew, J. P.; Burke, K.; Ernzerhof, M. Generalized Gradient Approximation Made Simple. *Phys. Rev. Lett.* **1996**, *77* (18), 3865–3868. https://doi.org/10.1103/PhysRevLett.77.3865.

(74) Grimme, S.; Ehrlich, S.; Goerigk, L. Effect of the Damping Function in Dispersion Corrected Density Functional Theory. *J. Comput. Chem.* **2011**, *32* (7), 1456–1465. https://doi.org/10.1002/jcc.21759.

(75) Hohenberg, P.; Kohn, W. Inhomogeneous Electron Gas. *Phys. Rev.* **1964**, *136* (3B), B864–B871. https://doi.org/10.1103/PhysRev.136.B864.

(76) Kohn, W.; Sham, L. J. Self-Consistent Equations Including Exchange and Correlation Effects. *Phys. Rev.* **1965**, *140* (4A), A1133–A1138. https://doi.org/10.1103/PhysRev.140.A1133.

(77) Nosé, S. A Molecular Dynamics Method for Simulations in the Canonical Ensemble. *Mol. Phys.* **1984**, *52* (2), 255–268. https://doi.org/10.1080/00268978400101201.

(78) Nosé, S. A Unified Formulation of the Constant Temperature Molecular Dynamics Methods. *J. Chem. Phys.* **1984**, *81* (1), 511-519. https://doi.org/10.1063/1.447334.

(79) Hoover. Canonical Dynamics: Equilibrium Phase-Space Distributions. *Phys. Rev. Gen. Phys.* **1985**, *31* (3), 1695–1697. https://doi.org/10.1103/physreva.31.1695.

(80) Mathew, K.; Kolluru, V. S. C.; Mula, S.; Steinmann, S. N.; Hennig, R. G. Implicit Self-Consistent Electrolyte Model in Plane-Wave Density-Functional Theory. *J. Chem. Phys.* **2019**, *151* (23), 234101. https://doi.org/10.1063/1.5132354.

(81) Petrosyan, S. A.; Rigos, A. A.; Arias, T. A. Joint Density-Functional Theory: Ab Initio Study of Cr_2O_3 Surface Chemistry in Solution. *J. Phys. Chem. B* **2005**, *109* (32), 15436–15444. https://doi.org/10.1021/jp044822k.

(82) Woodward, P. M.; Sleight, A. W.; Vogt, T. Structure Refinement of Triclinic Tungsten Trioxide. *J. Phys. Chem. Solids* **1995**, *56* (10), 1305–1315. https://doi.org/10.1016/0022-3697(95)00063-1.

(83) Loopstra, B. O.; Rietveld, H. M. Further Refinement of the Structure of WO_3. *Acta Crystallogr. Sect. B* **1969**, *25* (7), 1420–1421. https://doi.org/10.1107/S0567740869004146.

(84) Jin, H.; Zhu, J.; Hu, J.; Li, Y.; Zhang, Y.; Huang, X.; Ding, K.; Chen, W. Structural and Electronic Properties of Tungsten Trioxides: From Cluster to Solid Surface. *Theor. Chem. Acc.* **2011**, *130* (1), 103–114. https://doi.org/10.1007/s00214-011-0996-7.

(85) Wang, X.; Tian, F. H.; Zhao, W.; Fu, A.; Zhao, L. Surface Stabilization of Hexagonal WO_3 by Non-Metallic Atoms: A DFT Study. *Comput. Mater. Sci.* **2013**, *68*, 218–221. https://doi.org/10.1016/j.commatsci.2012.10.022.

(86) Zhu, J.; Wang, S.; Xie, S.; Li, H. Hexagonal Single Crystal Growth of WO_3 Nanorods along a [110] Axis with Enhanced Adsorption Capacity. *Chem. Commun.* **2011**, *47* (15), 4403. https://doi.org/10.1039/c1cc00064k.

(87) Oison, V.; Saadi, L.; Lambert-Mauriat, C.; Hayn, R. Mechanism of CO and O_3 Sensing on WO3 Surfaces: First Principle Study. *Sens. Actuators B Chem.* **2011**, *160* (1), 505–510. https://doi.org/10.1016/j.snb.2011.08.018.

(88) Lambert-Mauriat, C.; Oison, V.; Saadi, L.; Aguir, K. Ab Initio Study of Oxygen Point

Defects on Tungsten Trioxide Surface. *Surf. Sci.* **2012**, *606* (1–2), 40–45. https://doi.org/10.1016/j.susc.2011.08.018.

(89) Salje, E. The Orthorhombic Phase of WO_3. *Acta Crystallogr. B* **1977**, *33* (2), 574–577. https://doi.org/10.1107/S0567740877004130.

(90) Moscovici, J.; Rougier, A.; Laruelle, S.; Michalowicz, A. Apparent Mismatch between Extended X-Ray Absorption Fine Structure and Diffraction Structures of Crystalline Metastable WO_3 Phases. *J. Chem. Phys.* **2006**, *125* (12), 124505. https://doi.org/10.1063/1.2357148.

(91) Loopstra, B. O.; Rietveld, H. M. Further Refinement of the Structure of WO_3. *Acta Crystallogr. B* **1969**, *25* (7), 1420–1421. https://doi.org/10.1107/S0567740869004146.

(92) Szymanski, J. T.; Robert, A. C. The Crystal Structure of Tungstite, $WO_3.H_2O$. *Can. Mineral.* **1984**, *22* (4), 681–688.

(93) Villieras, F.; Cases, J. M.; Francois, M.; Michot, L. J.; Thomas, F. Texture and Surface Energetic Heterogeneity of Solids from Modeling of Low Pressure Gas Adsorption Isotherms. *Langmuir* **1992**, *8* (7), 1789–1795. https://doi.org/10.1021/la00043a018.

(94) Fowler, R. H. Statistical Thermodynamics. CUP Archive **1939**.

(95) Semmeq, A.; Foucaud, Y.; El Yamami, N.; Michailovski, A.; Lebègue, S.; Badawi, M. Hydration of Magnesite and Dolomite Minerals: New Insights from Ab Initio Molecular Dynamics. *Colloids Surf. Physicochem. Eng. Asp.* **2021**, *631*, 127697. https://doi.org/10.1016/j.colsurfa.2021.127697.

(96) Foucaud, Y.; Badawi, M.; Filippov, L. O.; Filippova, I. V.; Lebègue, S. Surface Properties of Fluorite in Presence of Water: An Atomistic Investigation. *J. Phys. Chem. B* **2018**, *122* (26), 6829–6836. https://doi.org/10.1021/acs.jpcb.8b02717.

(97) Ludwig, R. Water: From Clusters to the Bulk. *Angew. Chem. Int. Ed.* **2001**, *40* (10), 1808–1827. https://doi.org/10.1002/1521-3773(20010518)40:10<1808::AID-ANIE1808>3.0.CO;2-1.

(98) Maheshwary, S.; Patel, N.; Sathyamurthy, N.; Kulkarni, A. D.; Gadre, S. R. Structure and Stability of Water Clusters $(H_2O)_n$, $n = 8-20$: An Ab Initio Investigation. *J. Phys. Chem. A* **2001**, *105* (46), 10525–10537. https://doi.org/10.1021/jp013141b.

(99) Foucaud, Y.; Lebègue, S.; Filippov, L. O.; Filippova, I. V.; Badawi, M. Molecular Insight into Fatty Acid Adsorption on Bare and Hydrated (111) Fluorite Surface. *J. Phys. Chem. B* **2018**, *122* (51), 12403–12410. https://doi.org/10.1021/acs.jpcb.8b08969.

(100) Foucaud, Y.; Dufrêche, J.-F.; Siboulet, B.; Duvail, M.; Jonchère, A.; Diat, O.; Vuilleumier, R. Why Local and Non-Local Terms Are Essential for Second Harmonic Generation Simulation? *Phys. Chem. Chem. Phys.* **2022**, *24* (21), 12961–12973. https://doi.org/10.1039/D1CP05437F.

(101) Sokhan, V. P.; Tildesley, D. J. The Free Surface of Water: Molecular Orientation, Surface Potential and Nonlinear Susceptibility. *Mol. Phys.* **1997**, *92* (4), 625–640. https://doi.org/10.1080/002689797169916.

(102) Cipcigan, F. S.; Sokhan, V. P.; Jones, A. P.; Crain, J.; Martyna, G. J. Hydrogen Bonding and Molecular Orientation at the Liquid–Vapour Interface of Water. *Phys. Chem. Chem. Phys.* **2015**, *17* (14), 8660–8669. https://doi.org/10.1039/C4CP05506C.

TOC Graphic